ACS APPLIED MATERIALS & INTERFACES

Research Article

Cite This: ACS Appl. Mater. Interfaces 2019, 11, 47830−47836

www.acsami.org

Compositional Tailoring for Realizing High Thermoelectric Performance in Hafnium-Free n-Type ZrNiSn Half-Heusler Alloys

Nagendra S. Chauhan,[†,‡] Sivaiah Bathula,*[,†,‡,§] Bhasker Gahtori,[†,‡] Subhendra D. Mahanti,[∥] Amrita Bhattacharya,[⊥] Avinash Vishwakarma,[†,‡] Ruchi Bhardwaj,[†,‡] Vidya Nand Singh,[†] and Ajay Dhar*[,†,‡]

[†]Academy of Scientific & Innovative Research (AcSIR), CSIR-National Physical Laboratory (CSIR-NPL) Campus, New Delhi 110012, India

[‡]Advanced Materials & Devices Metrology Division, National Physical Laboratory, Council of Scientific and Industrial Research, New Delhi 110012, India

[§]School of Minerals, Metallurgical and Materials Engineering, Indian Institute of Technology Bhubaneswar, Bhubaneswar, Odisha 752050, India

[∥]Depatment of Physics & Astronomy, Michigan State University, Michigan 48824-1116, United States

[⊥]Department of Metallurgical Engineering and Material Science, Indian Institute of Technology Bombay, Mumbai, Maharashtra 400076, India

Supporting Information

ABSTRACT: Compositional tailoring enables fine-tuning of thermoelectric (TE) transport parameters by synergistic modulation of electronic and vibrational properties. In the present work, the aspects of compositionally tailored defects have been explored in ZrNiSn-based half-Heusler (HH) TE materials to achieve high TE performance and cost effectiveness in n-type Hf-free HH alloys. In off-stoichiometric Ni-rich $ZrNi_{1+x}Sn$ alloys in a low Ni doping limit ($x < 0.1$), excess Ni induces defects (Ni/vacancy antisite + interstitials), which tend to cause band structure modification. In addition, the structural similarity of HH and full-Heusler (FH) compounds and formation energetics lead to an intrinsic phase segregation of FH nanoscale precipitates that are coherently dispersed within the ZrNiSn HH matrix as nanoclusters. A consonance was achieved experimentally between these two competing mechanisms for optimal HH composition having both FH precipitates and Ni/vacancy antisite defects in the HH matrix by elevating the sintering temperature up to the solubility limit range of the ZrNiSn system. Defect-mediated optimization of electrical and thermal transport via carrier concentration tuning, energy filtering, and possibly all scale-hierarchical architecture resulted in a maximum $ZT \approx 1.1$ at 873 K for the optimized $ZrNi_{1.03}Sn$ composition. Our findings highlight the realistic prospect of enhancing TE performance via compositional engineering approach for wide applications of TE.

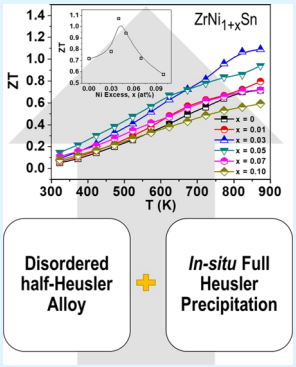

KEYWORDS: *half-Heusler, thermoelectric, defects, antisite defects, phase separation*

1. INTRODUCTION

In recent years, remarkable progress has been achieved for obtaining high thermoelectric (TE) performance by virtue of defect engineering[1−4] for synergistic optimization and effective decoupling of inter-related TE parameters. For the realization of high TE figure of merit (ZT) in a material, high electrical conductivity (σ), large Seebeck coefficient (α), and low thermal conductivity (κ) are necessary. From the application perspective in mid-temperature TE, ternary intermetallic (Ti, Zr, and Hf) NiSn-based half-Heusler (HH) class of materials is of great interest as potential n-type materials.[5−7] However, the essential use of expensive Hafnium has precluded its implementation in large-scale device applications. Thus, recent efforts have aimed at achieving high ZT in Hafnium-free HH alloys.[8−10]

As a distinctive advantage, HH alloys offer a tunable electronic structure, which can be modulated by doping/substitution/vacancy formation at any of its three metal sublattices, for engineering their narrow electronic band gap.[11−13] Thus, the high substitutability at all the three crystallographic sites in ternary HH alloys, particularly for (Ti, Zr, Hf) NiSn, which are narrow band gap semiconductors, has allowed the favorable tuning of electrical and thermal transport in the previously reported studies.[5,14−17]

In an extensive study by Makongo et al.,[17] in $Zr_{0.25}Hf_{0.75}Ni_{1+x}Sn$ (x = 0, 0.02, 0.05) and related alloys, a large increase in the thermopower as well as the electrical

Received: July 19, 2019
Accepted: August 23, 2019
Published: August 23, 2019

DOI: 10.1021/acsami.9b12599
ACS Appl. Mater. Interfaces 2019, 11, 47830−47836

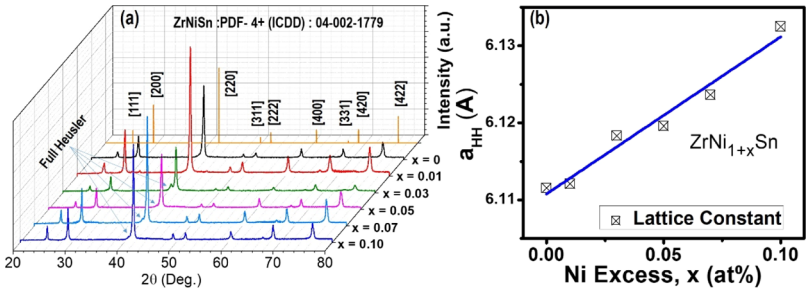

Figure 1. (a) XRD patterns and (b) lattice constant plotted as a function of excess Ni concentration (x) in $ZrNi_{1+x}Sn$ HH alloys.

conductivity of HH was observed simultaneously. This unusual behavior was ascribed to the coherent precipitation of nanometer-scale full-Heusler (FH) inclusions ($Zr_{0.25}Hf_{0.75}Ni_2Sn$) within the HH matrix ($Zr_{0.25}Hf_{0.75}NiSn$). The enhancements in the thermopower of the HH/FH nanocomposites was due to a reduction in the carrier concentration (n) around 300 K along with a simultaneous increase in the carrier mobility (μ), which compensated for the decrease in n without dramatically reducing the conductivity. The authors invoked an energy-filtering mechanism where the low-energy carriers are taken away from transport to understand this anomalous behavior. They also found that a favorable interplay between the temperature dependence of n and μ in the HH/FH nanocomposites resulted in large increases in the power factor (PF) at 775 K. Moreover, the embedded FH nanostructures also induced moderate reductions in the thermal conductivity κ_L caused by interface phonon scattering, leading to an increase in the ZT of HH$(1-x)$/FH(x) nanocomposites at 775 K.

In contrast to the above finding, our recent study[18] found that at an excess Ni doping of 3% in the HH compounds $ZrNi_{1+x}Sn$ (x = 0.03), the thermal conductivity reduced by more than 60% from that of the pure system (x = 0). A density functional theory-based analysis of the phonon band structure and scattering showed that at ultralow Ni doping, the localized vibrational modes of the antisite Ni defect played a very important role; they hybridized with the acoustic modes, resulting in the strong scattering of the thermal phonons, leading to a significant lowering in κ_L. At higher concentrations, however, the scattering of phonons from the interface of HH and FH nanoprecipitates also becomes important. Thus, both the antisite Ni defects and nanoprecipitates of FH in the HH matrix are present in the Ni-based HH compounds with excess Ni.

The above discussions clearly suggest that prior to undertaking the task of substitution by different types of elements for the optimization of TE properties in Ni-based HH compounds with excess Ni concentration, a deeper understanding of the nature of defects is essential in a simple system of ZrNiSn when we add excess Ni. Furthermore, recent electronic band structure studies[19,20] for different Ni contents in $ZrNi_{1+x}Sn$ revealed dramatic modifications of the electronic structure near the intrinsic band gap of ZrNiSn. For small x, isolated Ni defects introduced localized states in the gap which were modified when nanostructured FH clusters were introduced. These states are expected to play a significant role in the electronic properties of these Ni-based HH compounds with excess Ni, thereby affecting the PF. Thus, promising prospects of tuning the intrinsic structural defects (antisite, nanoprecipitates, etc.) for ZT enhancement in ZrNiSn alloys are possible via Ni-induced defect engineering.

In the present work, we study the role of Ni content in the low doping limit in enhancing the TE properties and achieving large ZT values in n-type Hf-free HH compositions. Synergistically optimized atomic-scale defects and the occurrence of intrinsic phase segregation of FH nanoscale precipitates favorably tune the TE transport, resulting in a state-of-the-art $ZT \approx 1.1$ at 873 K for optimized $ZrNi_{1.03}Sn$ HH composition, highlighting the realistic prospect of compositional engineering for the optimization of TE performance. Additionally, the constituent elements in $ZrNi_{1+x}Sn$ are earth-abundant, nontoxic, and relatively inexpensive, which in general is not the case for many state-of-the-art TE materials.

2. EXPERIMENTAL DETAILS

Polycrystalline $ZrNi_{1+x}Sn$ (x = 0−0.1) HH alloys were synthesized under an argon atmosphere by arc melting the stoichiometric amount of high-purity elements Zr (piece, 99.97%), Ni (powder, 99.97%), and Sn (shots, 99.98%). The ingots were remelted multiple times to ensure compositional homogeneity. Additional Sn was added to compensate for the loss in Sn because of evaporation during arc melting. The resulting arc-melted ingots were broken into small pieces and ground to a fine powder by using a mortar and pestle. The fine ground powders were then loaded into a graphite die with an inner diameter of 12.7 mm and compacted by spark plasma sintering at 1523 K under 50 MPa in a vacuum to obtain bulk dense pellets with relative densities > 98%. The Seebeck coefficient (α) and electrical resistivity (σ) were measured simultaneously, employing a commercial equipment (ULVAC, ZEM3), over the temperature range of 323−873 K on the samples of polished bars of about $3 \times 2 \times 10$ mm^3. Thermal conductivity (κ) was obtained using the equation $\kappa = \lambda \rho C_p$, where C_p is the specific heat capacity, ρ is the bulk density, and λ is the thermal diffusivity coefficient. Thermal diffusivity (λ) was measured with a laser flash technique (Lineseis, LFA 1000) on disk-shaped specimens of diameter 12.7 mm and thickness of 2.0 mm sprayed with a layer of graphite to minimize errors because of emissivity. Specific heat (C_p) was measured using a differential scanning calorimetry instrument. The volumetric density (ρ) was obtained using the Archimedes method (822e Mettler Toledo). The n and μ values were determined using the Hall effect measurement system (Nano-magnetics) under a magnetic field of 0.5 T. The accuracies in the transport measurement are: ±6% for thermal diffusivity, ±7% for electrical conductivity, ±7% for the Seebeck coefficient, ±10% for specific heat, and ±10% for density. The constituent phases were determined by X-ray diffraction (XRD; Rigaku Mini Flex II) using Cu Kα radiation (λ = 1.5406 Å). The morphology and elemental ratios of the synthesized samples are characterized by a field emission scanning electron microscope (Zeiss; model: Supra 40VP), whereas the microstructural examination was carried out using a high-resolution transmission electron microscope (HR-TEM model: Tecnai G2F30 STWIN operated at an electron accelerating voltage of 300 kV).

DOI: 10.1021/acsami.9b12599
ACS Appl. Mater. Interfaces 2019, 11, 47830−47836

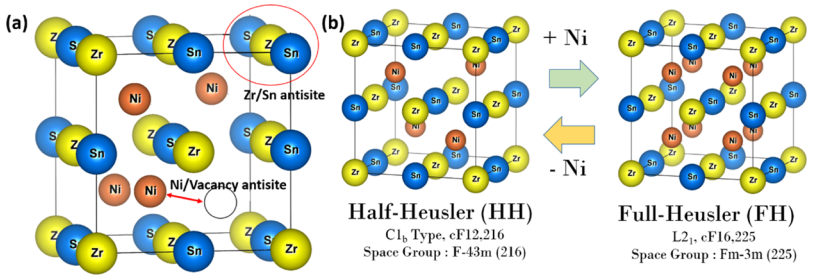

Figure 2. Schematic diagrams illustrating the (a) antisites in ZrNiSn and (b) structural similarity between the HH and FH phases.

3. RESULTS AND DISCUSSION

3.1. Structural Characterization. The XRD patterns of the synthesized $ZrNi_{1+x}Sn$ (x = 0−0.10) samples are shown in Figure 1a. The peaks seen in all the samples are well indexed with the ZrNiSn phase (structure type: $C1_b$; space group: 216, $F\bar{4}3m$) as the majority phase. For $x > 0.03$, the $ZrNi_2Sn$ phase (structure type: $L2_1$; space group: 225, $Fm\bar{3}m$) was observed as the minority phase, as indicated by a peak corresponding to the [220] plane. On the basis of the XRD profiles in Figure 1a, the lattice parameters (a_{HH}) were estimated and are shown in Figure 1b. The lattice constant of HH increases with an increasing Ni content, and the variation agrees fairly well with Vegard's law. The reported thermodynamic modeling[21] of Zr−Ni−Sn suggested a very low excess Ni solubility in ZrNiSn alloys even at high temperatures, whereas the Schultz−Scheil diagram,[21] for understanding the solidification behavior, revealed congruent melting for ZrNiSn at 1465 ± 10 °C and $ZrNi_2Sn$ at 1469 ± 10 °C. The linear increase in a_{HH} indicates a degree of excess Ni solubility in the HH matrix with an increasing Ni content, which suggests the occupancy of the vacant sites by excess Ni, resulting in Ni/vacancy antisites. This suggests the concurrence of Ni/vacancy antisites and in situ FH precipitation with the increasing Ni content. High computational time and cost, associated with the calculations of free energy for low x values, have limited the reported theoretical studies to $x > 0.1$ in (Ti, Zr)$Ni_{1+x}Sn$.[22] Thus, the possibility of limited excess Ni solubility ($0 < x < 0.1$) in $ZrNi_{1+x}Sn$ alloys could not be discarded, which can be addressed in future employing advanced computational capabilities. However, the reported experimental phase diagram studies indicate a narrow homogeneity region (within the range $0.02 \leq x \leq 0.06$ at 1223 K).[21,23] Thus, in any off-stoichiometric HH alloys with excess Ni, both the presence of Ni antisite defects as well as the phase separation of HH and FH alloys seem as distinct possibilities.

In ZrNiSn HH alloys, two kinds of antisite defects are likely to form during synthesis, namely Zr/Sn and Ni/vacancy antisites, as shown in Figure 2a.[14] Zr/Sn antisites are formed by the partial interchange of their sites because of the similarity in the atomic radii of Sn (1.58 Å) and Zr (1.60 Å) atoms, whereas Ni/vacancy antisites emerge from Ni migration to one of the four vacant Ni sites which can be considered as a generalized Ni/vacancy antisite. These structural imperfections are inherent features which are found even in stoichiometric compositions with modified lattice parameters. Previously reported ab initio κ calculations[16,20] have suggested that Ni-induced defects, that is, Ni/vacancy antisite defects and Ni interstitial defects, are energetically more favorable than Zr/Sn antisite defects. These defects control thermal transport, which was also experimentally demonstrated.[24] Thus, XRD analysis suggests the interstitial occupancy of Ni in $ZrNi_{1+x}Sn$, with the excess Ni occupying the interstitial tetrahedral site (Ni/vacancy antisite defects) in the HH structure in a manner similar to its analogue TiNiSn.[22,25,26] Besides HH, FH phase peaks were also observed within the XRD detection limit for $x \geq 0.05$, with the estimated lattice parameter a_{FH} = 6.28 Å. The Williamson−Hall analysis was used for the estimation of the crystallite size, which was found to be around 30−40 nm.

The field emission scanning electron microscopy (FE-SEM) images of a typical synthesized $ZrNi_{1.03}Sn$ HH alloy at a low magnification are shown in Figure 3a, which reveal a densely packed microstructure with the in situ FH precipitates. At a higher magnification, the equiaxed microstructure, shown in Figure 3b, exhibits a nanograined microstructure in both HH and FH regions, with the fine crystallites ∼10−30 nm, which is in close agreement to that estimated using the XRD data (Figure 1b). The elemental analysis carried out using energy-dispersive X-ray spectrometry (EDX) at regions marked as 1 and 2 in Figure 3c clearly identifies these regions as HH matrix and FH precipitates, respectively. The cross-sectional examination of the fractured surface by SEM also exhibits the precipitated FH within the HH matrix, as shown in Figure 3d. The EDX-based compositional analysis for all other synthesized samples is also shown in the Supporting Information (Figure S2).

To further investigate the microscopic features in the representative $ZrNi_{1.03}Sn$ HH alloy, high-resolution transmission electron microscopy (HR-TEM) analysis was performed in real and reciprocal space. Figure 3e presents the lattice-scale image of the nanostructured $ZrNi_{1.03}Sn$ alloy, which shows the presence of nanocrystallites with different orientations corresponding to both the HH and FH phases, having an average crystallite size ≈ 20 nm (similar to that calculated from the XRD patterns). The corresponding selected-area electron diffraction (SAED) pattern recorded for Figure 3f is shown as an inset, which also reveals the presence of the atomic planes of HH and FH in the reciprocal space. To further validate the in situ formation of FH precipitates, FE-SEM coupled with EDX elemental mapping was employed to probe a typical synthesized $ZrNi_{1.03}Sn$ HH alloy. Figure 4 shows the FE-SEM image, which indicates the various length scales of FH precipitates heterogeneously distributed in the ZrNiSn matrix, analogous to the observations reported earlier for similar alloy compositions.[27] The corresponding elemental maps (Figure 4) exhibit clear signatures of excess Ni, which can be ascribed to its presence in the FH precipitates. The implication of the observed microstructural features on TE transport is discussed in the subsequent sections.

3.2. TE Characterization. The temperature-dependent electronic transport properties of $ZrNi_{1+x}Sn$ (x = 0−0.10) HH

DOI: 10.1021/acsami.9b12599
ACS Appl. Mater. Interfaces 2019, 11, 47830−47836

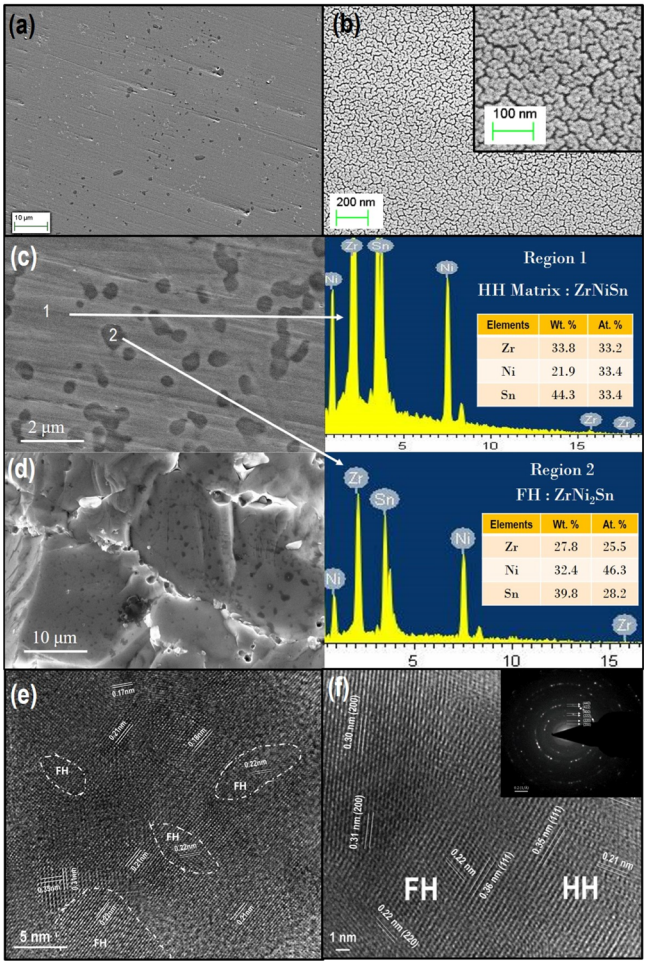

Figure 3. SEM image of typical $ZrNi_{1.03}Sn$ HH alloys at (a) low magnification showing dense microstructure and in situ FH precipitates and at (b) high magnification indicating nanostructured morphology; (c) low magnification along with the EDX analysis of regions marked as regions 1 and 2; (d) cross-sectional view; HR-TEM image showing (e) lattice-scale image of nanostructured $ZrNi_{1.03}Sn$, exhibiting the presence of different orientations of the crystallographic planes corresponding to the HH and FH phases and their interface boundary images; (f) regions of semicoherent HH and FH phases along with the corresponding SAED patterns shown in the inset confirming the polycrystalline microstructure.

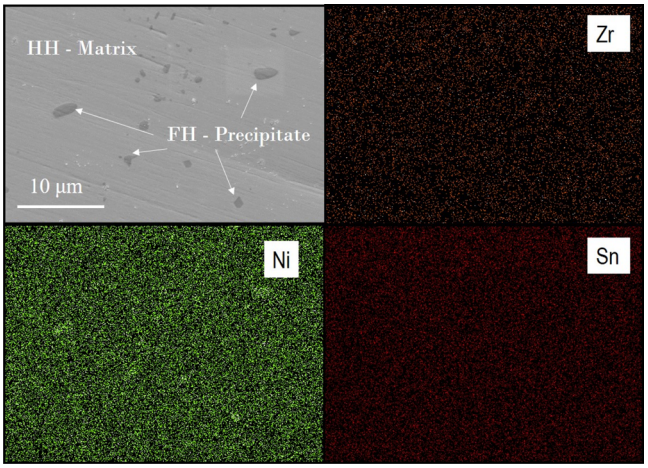

Figure 4. SEM micrograph indicating FH precipitation along with the elemental mapping of the constituent elements of the $ZrNi_{1.03}Sn$ HH alloy.

alloys are shown in Figure 5a. The electrical conductivity (σ) in all samples increases with increasing temperature, indicating a typical semiconducting behavior. At 323 K, up to 170% enhancement in σ of $ZrNi_{1.1}Sn$ ($\sim 5.7 \times 10^4$ S m^{-1}) was observed when compared with pristine ZrNiSn ($\sim 2.1 \times 10^4$ S m^{-1}). At higher temperatures, σ was also found to increase, but by a smaller amount, by ~30% in $ZrNi_{1.1}Sn$ (1.2×10^5 S m^{-1}) compared to the pristine ZrNiSn (9.0×10^4 S m^{-1}), similar to the observations made previously[28] at similar temperatures. With an increasing Ni content (x), σ initially decreases for $x <$ 0.03 and increases thereafter. The implication of excess Ni on electrical transport can be understood using room-temperature Hall measurements, as shown in Table 1.

The carrier mobility (μ) in all the samples with excess Ni was found to increase with an increasing Ni content, as shown in Table 1. The increase in μ can be attributed to the presence of metallic FH nanoclusters which provide an easy path for the carriers to take part in the electron transport, in a manner similar to that in earlier reports.[9,17,29] Interestingly, in compositions with a lower concentration of excess Ni, n decreases and μ increases. The decrease in n is unusual, as the presence of metallic FH nanoclusters within a semiconducting HH matrix should generally increase the carrier density of the resulting FH/HH pseudobinary composite. However, the nonmonotonic dependence of electrical conductivity and n was similar to that in previous reports,[17] which suggest that the observed reduction in n can be attributed to the phenomena of energy filtering of carriers, dominant at a lower concentration of Ni (x) in $ZrNi_{1+x}Sn$. The effect of antisite defects and FH nanoclusters on n and μ (Figure 3) can be qualitatively understood as follows. The former can localize the carriers (by creating localized states in the band gap which act as electron traps), whereas the latter tend to generate energy barriers at the phase boundaries between the HH matrix and the FH nanoclusters, causing band bending,[30] resulting in a lower μ of carriers of lower energy, which can appear effectively as a lower n. Thus, the selective filtering of low-mobility and low-energy carriers at the FH/HH interfaces allows only high-mobility and high-energy majority charge carriers (electrons) to pass through, which improves σ, despite a reduction in n, as observed by the Hall measurements (Table 1). The magnitude of the bending potential at the HH/FH interface is largely dependent on the size of the precipitates and the interfacial properties between the matrix and the precipitates, which in case of smaller FH precipitates (prominent in lower excess Ni compositions) favors a larger bending potential with an increased carrier filtering probability. Thus, an increase in the Ni content results in an increase in n with a diminishing effect of carrier filtering because of larger precipitates with lowering bending potential. Additionally, the presence of Ni/vacancy antisites, as expected, will contribute additional carriers locally, resulting in self-doping with the localized charge carriers.

Figure 5b shows the temperature dependence of the Seebeck coefficient (α). The negative sign of α confirms the dominance of electrons in charge transport. At 323 K, the magnitudes of α in all samples with excess Ni (up to $x = 0.07$) were found to be enhanced, with the highest α of 237 μV K^{-1} measured for $ZrNi_{1.03}Sn$ [which is 30% higher than α of the pristine ZrNiSn (185 μV K^{-1})]. The improvement can be understood in terms

DOI: 10.1021/acsami.9b12599
ACS Appl. Mater. Interfaces 2019, 11, 47830−47836

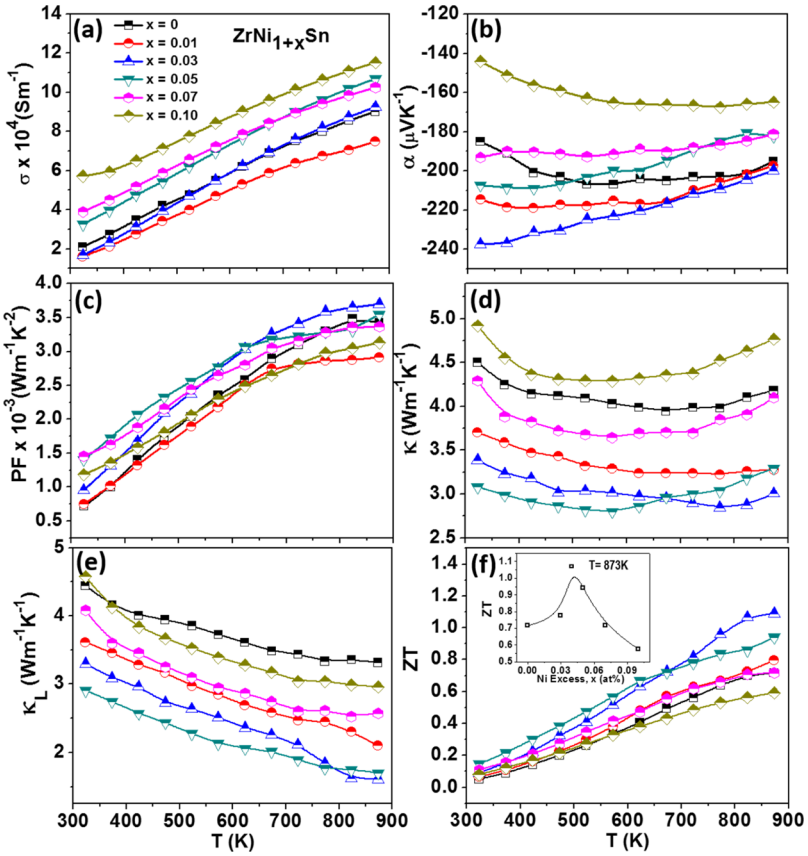

Figure 5. Temperature dependence of (a) electrical conductivity, (b) Seebeck coefficient (c) PF, (d) thermal conductivity, (e) lattice thermal conductivity, and (f) TE figure of merit (ZT); inset: ZT vs excess Ni content of the $ZrNi_{1+x}Sn$ (x = 0–0.1) HH alloy.

Table 1. Physical Parameters of HH $ZrNi_{1+x}Sn$ at Room Temperature

	x = 0	x = 0.01	x = 0.03	x = 0.05	x = 0.07	x = 0.10
ρ (Ohm m)	6.40×10^{-5}	7.80×10^{-5}	6.58×10^{-5}	5.50×10^{-5}	4.58×10^{-5}	3.67×10^{-5}
R_H (m^3 C^{-1})	1.36×10^{-7}	1.66×10^{-7}	1.80×10^{-7}	1.63×10^{-7}	1.35×10^{-7}	1.14×10^{-7}
n (cm^{-3})	4.87×10^{19}	3.76×10^{19}	3.47×10^{19}	3.84×10^{19}	4.61×10^{19}	5.46×10^{19}
μ_H (cm^2 V^{-1} s^{-1})	22.35	24.41	27.36	29.63	33.10	34.8
α (μV K^{-1})	−178	−205	−217	−201	−183	−138

of the inverse dependence of α with n. For compositions 0.01 > x > 0.07 in $ZrNi_{1+x}Sn$, higher α was observed than that for the pristine ZrNiSn, which diminishes at elevated temperatures because of the changing interfacial characteristics between the HH matrix and FH precipitates along with the thermal excitation of minority charge carriers resulting in bipolar transport. With an increasing temperature, the gradual reduction of α can be attributed to the gradual loss of the band bending potential at the HH/FH interface, which is insufficient to filter the low-energy carriers.

The temperature dependence of PF is shown in Figure 5c. Compared to the pristine ZrNiSn sample, the samples with excess Ni show enhanced PF up to x = 0.07, above which because of the increased n, α deteriorates. Thus, the substantial α and the sizable enhancement in σ result in the PF of ~1 × 10^{-3} W m^{-2} K^{-1} at 323 K and around ~3.6 × 10^{-3} W m^{-2} K^{-1} at 873 K for 0.03 ≤ x ≤ 0.07. A maximum PF of 3.7 × 10^{-3} W m^{-2} K^{-1} was achieved for the composition $ZrNi_{1.03}Sn$.

Figure 5d shows the temperature-dependent total thermal conductivity (κ) of $ZrNi_{1+x}Sn$, which is calculated using the measured thermal diffusivity (λ), specific heat (C_p), and density, as shown in the Supporting Information (Figure S1). The λ value decreases with increasing Ni doping concentration up to $x \leq 0.05$ and increases thereafter. In the low-temperature range, λ decreases with increasing temperature for all samples but increases thereafter at higher temperature because of the intrinsic excitation of charge carriers. The intrinsic excitation of carriers at higher temperatures results in an increased bipolar conduction (because of minority charge carriers) and κ_e (because of majority charge carriers), both of which contribute toward increasing κ in the higher temperature range, as observed in Figure 5d. In the low Ni doping limit (x < 0.07), the values of κ of all the samples were found to drastically reduce in the measured temperature range. To understand this reduction in κ, electronic thermal conductivity (κ_e) and lattice thermal conductivity (κ_L) were estimated using the Wiedemann–Franz Law with α-dependent Lorenz number[31] and using the relation $\kappa_L = \kappa - \kappa_e$. The calculated Lorenz number was found to be in the range of (1.6–1.8) × 10^{-8} V^2 K^{-2}.

On the basis of our theoretical study reported earlier,[18] in addition to the interfacial defects at HH/FH, the enhanced phonon scattering in the lower doping limit is largely associated with Ni-induced antisite defects. The κ_L value, as shown in Figure 5e, decreases with an increasing Ni content up

DOI: 10.1021/acsami.9b12599
ACS Appl. Mater. Interfaces 2019, 11, 47830–47836

to ($x < 0.05$) and increases thereafter. At 323 K, in the ultralow Ni doping regime ($x < 0.05$) in the ZrNiSn lattice, κ_L is substantially reduced. Although κ_L contributes majorly to κ, the κ_e contribution to κ becomes considerable only in high Ni concentration compositions and at higher temperatures. The measured C_p was found to be ~10% lower for the pristine ZrNiSn than that estimated theoretically[20,32] based on the Dulong–Petit law and reported experimentally[7,33,34] for similar compositions. This observed reduction in C_p can be explained by the presence of localized modes of the antisite Ni defects, which hybridize with the acoustic modes of the HH lattice and result in an enhanced scattering of the thermal phonons.[18,35] This leads to a significant lowering of phonon contribution to C_p, which is also evidenced by significant lowered κ_L. It is observed that for temperature above the Debye temperature, C_p shows a marginal variation, which is in close proximity to the Dulong–Petit limit (~24.94 within ±0.04 J mol^{-1} K^{-1} $atom^{-1}$ at 2000 K),[20,34] for all the synthesized ZrNiSn samples, which can be attributed to the anharmonicity, phase instability, and intrinsic disorder observed in ZrNiSn. The increase in C_p with Ni concentration can be because of the increasing electronic contribution to C_p because of high σ. The significant variation in the thermal transport parameters for the disordered ZrNiSn HH alloy has been understood in detail by the theory–experiment comparison of the dependence of κ_L on temperature and crystallite size.[32] Among the dominant phonon scattering mechanisms responsible for the reduction in the κ_L value of HH, the grain boundary scattering rather than localized point defect scattering was found to be majorly responsible, causing the spread in κ_L values reported previously for ZrNiSn.[32]

It is noteworthy that in the present study, κ_L for all the samples containing excess Ni concentration compositions is significantly lower than that for the pristine ZrNiSn for the entire temperature range.[12,32,33] The observed phonon dynamics can be ascribed to the presence of characteristic intrinsic disorder in ZrNiSn alloys, in situ formed FH precipitates, antisites, and nanosized grains. At 873 K, the lowest values of $\kappa_L \approx 1.67$ W m^{-1} K^{-1} and $\kappa \approx 3.0$ W m^{-1} K^{-1} were achieved in the composition $ZrNi_{1.03}Sn$, which correspond to ~40 and 30% reduction, respectively, compared to its pristine counterpart. The interfacial defects at HH/FH contribute to phonon scattering and become increasingly important at lower x values, wherein the presence of all-scale FH precipitates is more prominent for the scattering of phonons with a wide range of frequencies (energies) or mean free path. Thus, in the synthesized FH/HH nanocomposites, point defects, strain, dislocations, and nanostructures jointly contribute to significantly increase the strength of the phonon scattering which decreases κ significantly.

The temperature dependence of ZT is shown in Figure 5f, where an enhancement in ZT is observed for all the samples with excess Ni with an enhanced $ZT \approx 1.1$ at 873 K for $ZrNi_{1.03}Sn$, owing to the synergistic improvement in PF combined with drastically reduced κ. On increasing the value of x beyond 0.07, the enhancement in the PF and ZT values begins to decrease as n becomes too large, which drastically reduces α. As a result, the highest ZT of ~1.1 has been attained at 873 K in samples from $x = 0.03$ to 0.05, which corresponds to a 25% increase over the stoichiometric ZrNiSn with optimized doping.

4. CONCLUSIONS

In summary, an attempt to improve the TE performance in ZrNiSn HH alloys by compositional engineering has led to the achievement of state-of-the-art $ZT \approx 1.1$ at 873 K, for $ZrNi_{1.03}Sn$, which is found to be the highest among hafnium-free HH alloys till date, to the best of our knowledge. It was found that at ultralow Ni doping in ZrNiSn, both FH precipitates and Ni-induced defects (Ni/vacancy antisite + interstitials) exist in the HH matrix, which favorably tune the thermal and electrical transport. The occurrence of carrier localization and energy filtering of carriers at FH/HH interfaces tend to increase the PF. The presence of localized vibrational modes of Ni antisite defects and FH precipitates effectively scatters the heat-carrying phonons and cause an appreciable reduction in κ. Thus, we believe that controlling the structural imperfections through compositional engineering at different length scales in HH materials provides an effective paradigm for improving and optimizing their TE properties.

■ ASSOCIATED CONTENT

Supporting Information

The Supporting Information is available free of charge at https://pubs.acs.org/doi/10.1021/acsami.9b12599.

Thermal transport parameters and structural characterization of $ZrNi_{1+x}Sn$ HH alloys (PDF)

■ AUTHOR INFORMATION

Corresponding Authors

*E-mail: sivaiahb@iitbbs.ac.in; Phone: +91 674 713 6914 (S.B.)

*E-mail: adhar@nplindia.org (A.D.)

ORCID

Nagendra S. Chauhan: 0000-0003-2579-6642

Sivaiah Bathula: 0000-0001-6093-6351

Ajay Dhar: 0000-0001-7494-0378

Notes

The authors declare no competing financial interest.

■ ACKNOWLEDGMENTS

The authors sincerely acknowledge BRNS, India, for the financial support (grant no: 37(3)/14/22/2016-BRNS). N.S.C. acknowledges the financial support from CSIR-India (grant no: 31/001(0430)/2014-EMR-1). The technical support rendered by Radhey Shyam and Naval Kishor Upadhyay is also gratefully acknowledged.

■ REFERENCES

(1) Li, Z.; Xiao, C.; Zhu, H.; Xie, Y. Defect chemistry for thermoelectric materials. *J. Am. Chem. Soc.* **2016**, *138*, 14810–14819.

(2) Hu, L.; Zhu, T.; Liu, X.; Zhao, X. Point Defect Engineering of High-Performance Bismuth-Telluride-Based Thermoelectric Materials. *Adv. Funct. Mater.* **2014**, *24*, 5211–5218.

(3) Pei, Y.; Wang, H.; Snyder, G. J. Band engineering of thermoelectric materials. *Adv. Mater.* **2012**, *24*, 6125–6135.

(4) Chai, Y. W.; Yoshioka, K.; Kimura, Y. Intrinsic point defects in thermoelectric half-Heusler alloys. *Scr. Mater.* **2014**, *83*, 13–16.

(5) Chen, S.; Ren, Z. Recent progress of half-Heusler for moderate temperature thermoelectric applications. *Mater. Today* **2013**, *16*, 387–395.

(6) Sakurada, S.; Shutoh, N. Effect of Ti substitution on the thermoelectric properties of (Zr, Hf) NiSn half-Heusler compounds. *Appl. Phys. Lett.* **2005**, *86*, 082105.

DOI: 10.1021/acsami.9b12599
ACS Appl. Mater. Interfaces 2019, 11, 47830–47836

(7) Joshi, G.; Yan, X.; Wang, H.; Liu, W.; Chen, G.; Ren, Z. Enhancement in thermoelectric figure-of-merit of an N-type half-Heusler compound by the nanocomposite approach. *Adv. Energy Mater.* **2011**, *1*, 643−647.
(8) Chauhan, N. S.; Bathula, S.; Vishwakarma, A.; Bhardwaj, R.; Gahtori, B.; Kumar, A.; Dhar, A. Vanadium-Doping-Induced Resonant Energy Levels for the Enhancement of Thermoelectric Performance in Hf-Free ZrNiSn Half-Heusler Alloys. *ACS Appl. Energy Mater.* **2018**, *1*, 757−764.
(9) Chauhan, N. S.; Bhardwaj, A.; Senguttuvan, T. D.; Pant, R. P.; Mallik, R. C.; Misra, D. K. A synergistic combination of atomic scale structural engineering and panoscopic approach in p-type ZrCoSb-based half-Heusler thermoelectric materials for achieving high ZT. *J. Mater. Chem. C* **2016**, *4*, 5766−5778.
(10) Chauhan, N. S.; Bathula, S.; Vishwakarma, A.; Bhardwaj, R.; Gahtori, B.; Srivastava, A. K.; Saravanan, M.; Dhar, A. A nano-composite approach for enhancement of thermoelectric performance in Hafnium-free Half-Heuslers. *Materialia* **2018**, *1*, 168.
(11) Hohl, H.; Ramirez, A. P.; Goldmann, C.; Ernst, G.; Wölfing, B.; Bucher, E. Efficient dopants for ZrNiSn-based thermoelectric materials. *J. Phys.: Condens. Matter* **1999**, *11*, 1697.
(12) Muta, H.; Kanemitsu, T.; Kurosaki, K.; Yamanaka, S. Substitution effect on thermoelectric properties of ZrNiSn based half-Heusler compounds. *Mater. Trans.* **2006**, *47*, 1453−1457.
(13) Zeier, W. G.; Schmitt, J.; Hautier, G.; Aydemir, U.; Gibbs, Z. M.; Felser, C.; Snyder, G. J. Engineering half-Heusler thermoelectric materials using Zintl chemistry. *Nat. Rev. Mater.* **2016**, *1*, 16032.
(14) Zhu, T.; Fu, C.; Xie, H.; Liu, Y.; Zhao, X. High Efficiency Half-Heusler Thermoelectric Materials for Energy Harvesting. *Adv. Energy Mater.* **2015**, *5*, 1500588.
(15) Chauhan, N. S.; Bathula, S.; Vishwakarma, A.; Bhardwaj, R.; Johari, K. K.; Gahtori, B.; Saravanan, M.; Dhar, A. Compositional tuning of ZrNiSn half-Heusler alloys: Thermoelectric characteristics and performance analysis. *J. Phys. Chem. Solids* **2018**, *123*, 105.
(16) Katre, A.; Carrete, J.; Mingo, N. Unraveling the dominant phonon scattering mechanism in the thermoelectric compound ZrNiSn. *J. Mater. Chem. A* **2016**, *4*, 15940−15944.
(17) Makongo, J. P. A.; Misra, D. K.; Zhou, X.; Pant, A.; Shabetai, M. R.; Su, X.; Uher, C.; Stokes, K. L.; Poudeu, P. F. P. Simultaneous large enhancements in thermopower and electrical conductivity of bulk nanostructured half-Heusler alloys. *J. Am. Chem. Soc.* **2011**, *133*, 18843−18852.
(18) Chauhan, N. S.; Gahtori, B.; Sivaiah, B.; Mahanti, S. D.; Dhar, A.; Bhattacharya, A. Modulating the lattice dynamics of n-type Heusler compounds via tuning Ni concentration. *Appl. Phys. Lett.* **2018**, *113*, 013902.
(19) Do, D. T.; Mahanti, S. D.; Pulikkoti, J. J. Electronic structure of Zr−Ni−Sn systems: role of clustering and nanostructures in half-Heusler and Heusler limits. *J. Phys.: Condens. Matter* **2014**, *26*, 275501.
(20) Page, A.; Uher, C.; Poudeu, P. F.; Van der Ven, A. Phase separation of full-Heusler nanostructures in half-Heusler thermoelectrics and vibrational properties from first-principles calculations. *Phys. Rev. B: Condens. Matter Mater. Phys.* **2015**, *92*, 174102.
(21) Sauerschnig, P.; Grytsiv, A.; Vrestal, J.; Romaka, V.; Smetana, B.; Giester, G.; Bauer, E.; Rogl, P. On the constitution and thermodynamic modelling of the system Zr-Ni-Sn. *J. Alloys Compd.* **2018**, *742*, 1058.
(22) Tang, Y.; Li, X.; Martin, L. H. J.; Cuervo Reyes, E.; Ivas, T.; Leinenbach, C.; Anand, S.; Peters, M.; Snyder, G. J.; Battaglia, C. Impact of Ni content on the thermoelectric properties of half-Heusler TiNiSn. *Energy Environ. Sci.* **2018**, *11*, 311−320.
(23) Gürth, M.; Grytsiv, A.; Vrestal, J.; Romaka, V. V.; Giester, G.; Bauer, E.; Rogl, P. On the constitution and thermodynamic modelling of the system Ti−Ni−Sn. *RSC Adv.* **2015**, *5*, 92270−92291.
(24) Xie, H.-H.; Mi, J.-L.; Hu, L.-P.; Lock, N.; Chirstensen, M.; Fu, C.-G.; Iversen, B. B.; Zhao, X.-B.; Zhu, T.-J. Interrelation between atomic switching disorder and thermoelectric properties of ZrNiSn half-Heusler compounds. *CrystEngComm* **2012**, *14*, 4467−4471.
(25) Douglas, J. E.; Chater, P. A.; Brown, C. M.; Pollock, T. M.; Seshadri, R. Nanoscale structural heterogeneity in Ni-rich half-Heusler TiNiSn. *J. Appl. Phys.* **2014**, *116*, 163514.
(26) Kirievsky, K.; Gelbstein, Y.; Fuks, D. Phase separation and antisite defects in the thermoelectric TiNiSn half-Heusler alloys. *J. Solid State Chem.* **2013**, *203*, 247−254.
(27) Romaka, V. V.; Rogl, P.; Romaka, L.; Stadnyk, Y.; Grytsiv, A.; Lakh, O.; Krayovskii, V. Peculiarities of structural disorder in Zr-and Hf-containing Heusler and half-Heusler stannides. *Intermetallics* **2013**, *35*, 45−52.
(28) Chai, Y. W.; Oniki, T.; Kimura, Y. Microstructure and thermoelectric properties of a ZrNi1. 1Sn half-Heusler alloy. *Acta Mater.* **2015**, *85*, 290−300.
(29) Xie, W. J.; He, J.; Zhu, S.; Su, X. L.; Wang, S. Y.; Holgate, T.; Graff, J. W.; Ponnambalam, V.; Poon, S. J.; Tang, X. F. Simultaneously optimizing the independent thermoelectric properties in (Ti, Zr, Hf)(Co, Ni) Sb alloy by in situ forming InSb nanoinclusions. *Acta Mater.* **2010**, *58*, 4705−4713.
(30) Faleev, S. V.; Léonard, F. Theory of enhancement of thermoelectric properties of materials with nanoinclusions. *Phys. Rev. B: Condens. Matter Mater. Phys.* **2008**, *77*, 214304.
(31) Kim, H.-S.; Gibbs, Z. M.; Tang, Y.; Wang, H.; Snyder, G. J. Characterization of Lorenz number with Seebeck coefficient measurement. *APL Mater.* **2015**, *3*, 041506.
(32) Schrade, M.; Berland, K.; Eliassen, S. N.; Guzik, M. N.; Echevarria-Bonet, C.; Sørby, M. H.; Jenuš, P.; Hauback, B. C.; Tofan, R.; Gunnæs, A. E. The role of grain boundary scattering in reducing the thermal conductivity of polycrystalline X NiSn (X= Hf, Zr, Ti) half-Heusler alloys. *Sci. Rep.* **2017**, *7*, 13760.
(33) Xie, H.; Wang, H.; Fu, C.; Liu, Y.; Snyder, G. J.; Zhao, X.; Zhu, T. The intrinsic disorder related alloy scattering in ZrNiSn half-Heusler thermoelectric materials. *Sci. Rep.* **2014**, *4*, 6888.
(34) Wang, H.; Bai, S.; Chen, L.; Cuenat, A.; Joshi, G.; Kleinke, H.; König, J.; Lee, H. W.; Martin, J.; Oh, M.-W.; Porter, W. D.; Ren, Z.; Salvador, J.; Sharp, J.; Taylor, P.; Thompson, A. J.; Tseng, Y. C. International round-robin study of the thermoelectric transport properties of an n-Type half-heusler compound from 300 K to 773 K. *J. Electron. Mater.* **2015**, *44*, 4482−4491.
(35) Andritsos, E. I.; Zarkadoula, E.; Phillips, A. E.; Dove, M. T.; Walker, C. J.; Brazhkin, V. V.; Trachenko, K. The heat capacity of matter beyond the Dulong−Petit value. *J. Phys.: Condens. Matter* **2013**, *25*, 235401.

DOI: 10.1021/acsami.9b12599
ACS Appl. Mater. Interfaces 2019, 11, 47830−47836